Coexistence of transient liquid droplets and amorphous solid particles in nonclassical crystallization of cerium oxalate

Maxime Durelle, Sophie Charton, Frédéric Gobeaux, Corinne Chevallard, Luc Belloni, Fabienne Testard, Sylvain Trépout, David Carriere

Coexistence of Transient Liquid Droplets and Amorphous Solid Particles in Non-classical Crystallization of Cerium Oxalate

Maxime Durelle,[†,‡] Sophie Charton,[†] Frédéric Gobeaux,[‡] Corinne Chevallard,[‡] Luc Belloni,[‡] Fabienne Testard,[‡] Sylvain Trépout,[¶,§] and David Carriere[*,‡]

†*CEA, DES, ISEC, DMRC, Univ. Montpellier, 30207, Marcoule, France*

‡*Université Paris-Saclay, CNRS, CEA, NIMBE, LIONS, 91191, Gif-sur-Yvette, France*

¶*Institut Curie, Université PSL, CNRS UMS2016, Inserm US43, Université Paris-Saclay, Multimodal Imaging Center, 91400 Orsay, France*

§*Current address: Monash University, Ramaciotti Centre for Cryo-EM, Clayton Campus, 3800 Victoria, Australia*

E-mail: david.carriere@cea.fr

Abstract

Crystallization from solution often occurs via "non-classical" routes, i.e. involves transient, non crystalline states like reactant-rich liquid droplets and amorphous particles. However, in mineral crystals, the well-defined thermodynamic character of liquid droplets, and whether they convert - or not - into amorphous phases has remained unassessed. Here, by combining cryo-transmission electron microscopy and X-ray scattering down to 250 ms reaction time, we unveil that crystallization of cerium oxalate involves a metastable chemical equilibrium between transient liquid droplets and solid amorphous particles: contrarily to an usual expectation, reactant-rich droplets do not evolve into amorphous solids. Instead, at concentrations above 2.5 to 10 $\mathrm{mmol\,L^{-1}}$, both amorphous and reactant-rich liquid phases coexist for several tens of seconds, their molar fractions remain constant, and follow the lever rule in a multicomponent phase diagram. Such metastable chemical equilibrium between solid and liquid precursors has been so far overlooked in multistep nucleation theories, and highlight the interest of rationalizing phase transformations using multicomponent phase diagrams not only when designing and recycling rare earths materials, but more generally when describing non-classical crystallization.

Graphical TOC Entry

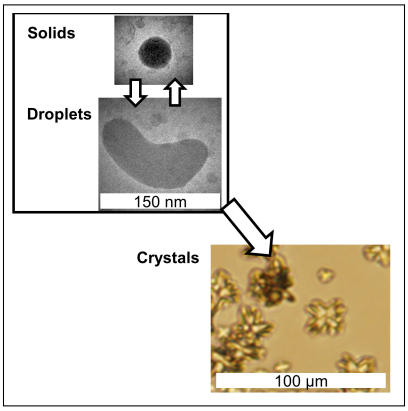

Keywords

Non-classical nucleation, rare-earth oxalate, SAXS, cryo-TEM

Crystallization of ions from aqueous solutions is ubiquitous, both in natural and industrial processes (biomineralization, lithogenesis, scaling, materials synthesis). The scientific interest in crystallization is motivated not only by a tremendous practical importance, but also by recent awareness that crystal emergence is far from understood. Indeed, crystallization remains depicted by the well-known classical nucleation theory (CNT),[1–3] which considers that crystalline clusters fluctuate in size by addition and removal of "monomers", and finally overcome a nucleation barrier: clusters sometimes grow above a critical size, where the probability to further grow increases steeply with size, leading finally to macroscopic-sized clusters. This nucleation / growth scenario remains largely used in models of industrial-scale precipitation,[4] despite its appropriateness being questioned by experimental observations. Indeed, CNT assumes that clusters have the same structural properties as the bulk crystal. This assumption is contradicted by large experimental evidence of transient non-crystalline states prior to crystallization,[5] such as amorphous particles or networks,[6–8] or liquid droplets rich in solutes that separate from water via a liquid-liquid phase separation (LLPS).[9–18]

LLPS is acknowledged as a potential unifying concept: its description by classical theories for nucleation and spinodal decomposition has provided rational guidelines in the field of protein crystallization where LLPS is common.[11,19,20] Rationalization of LLPS opens similar perspectives for inorganic crystals, but its generic character needs further assessment. Indeed, "mineral emulsions" were previously described as out-of-equilibrium patterns,[21,22] with ill-defined chemical compositions dependent on the mixing process, but not described by an underlying phase diagram. Based on post-synthesis size analyses of solid particles, Faatz *et al.* have postulated a liquid-liquid binodal line in $CaCO_3$ aqueous syntheses ,[23] and mineral emulsions of $CaCO_3$ have since gained the status of a thermodynamic phase, well-defined in composition, that forms by nucleation or spinodal decomposition, then forms amorphous particles.[15–17,23–28] The consecutive formation of reactant-rich droplets, amorphous particles, and crystals, each with well-defined thermodynamic parameters (solubilities), allows a licit use of the multistep nucleation theory, which is the state-of-the-art rationalization of non-

classical crystallization:[19] each new phase (liquid droplets, amorphous particles, or crystals) nucleates from its respective parent phase following the classical nucleation theory.

It is indeed clear that amorphous calcium carbonate is a true phase with well-defined thermodynamic parameters (structure, chemical composition). However, the transformation of the reactant-rich liquid is still poorly characterized, which makes the thermodynamic status mineral-rich droplets unclear, even for calcium carbonate: on the one hand, the liquid binodal line has been identified at calcium concentrations around $1 \times 10^{-4}\,\mathrm{mol\,L^{-1}}$,[15] and the spinodal around $3 \times 10^{-3}\,\mathrm{mol\,L^{-1}}$, either with an upper critical point above 340 K,[28] or a lower critical point in the 100-283 K range.[23,29] On the other hand, the phase boundaries must be determined before amorphous and / or crystalline particles form, which limits the accessible concentration ranges (supersaturations) and available characterization techniques. Current conclusions have therefore to rely on incomplete information on the nature and amount of phases, and mostly, hypothesize that the reactant-rich liquid converts into amorphous particles.[15,18,23,26,29–31]

To test the generality of conclusions on mineral LLPS, we study here the co-precipitation of cerium oxalate decahydrate ($Ce_2(C_2O_4)_3 \cdot 10\,H_2O$) in water. Cerium oxalate not only shows a practical interest, being a model for rare-earth and actinides recycling,[32,33] and a precursor of cerium oxide nanoparticles for energy-related applications, such as electrocatalysis,[34,35] but also involves non-classical crystallization *via* amorphous particles, and possibly liquid structures.[8,36] Here, we combine cryo-TEM morphology observations and an analysis of X-ray scattering properties of the solution down to 250 ms after mixing the reactants and show not only that both amorphous particles and liquid droplets form, but also that they coexist at cerium concentrations above 2.5 to 10 $\mathrm{mmol\,L^{-1}}$. Both amorphous and liquid phases lack long-range crystal order; however, the liquid phase is characterized by i) a distinct and lower X-ray scattering efficiency, consistent with a larger molar volume and / or water content, and ii) droplet morphology with curved shapes, evidencing qualitatively a lower viscosity and / or a lower interfacial tension. Prior to crystallization of cerium oxalate, we find no

evidence of conversion of either phase into another: the volume fractions of each phase are constant and consistent with a phase diagram lever rule, evidencing a metastable chemical equilibrium between intermediate phases.

We have synthesized crystals by mixing aqueous solutions of cerium nitrate and oxalic acid in stoichiometric conditions *via* a custom-made millifluidic mixer.[37] With [Ce] = 1 mmol L^{-1} and 5 s after mixing, we observe transient amorphous nanoparticles by cryo-TEM as aggregated cerium- and oxygen-rich spherical particles with sizes of a few tens of nanometers (Fig. 1a-d, SI 2.1, tomography in Movie SM1.avi, and Electron Energy Loss Spectroscopy (EELS) SI 3.1). Amorphous nanoparticles are evidenced by Small to Wide Angle X-ray Scattering (SAXS/WAXS) at reaction times of 250 ms (Fig. 2a): the plateau followed by a decay at $q \simeq 2 \times 10^{-2}$ Å^{-1} is characteristic of polydisperse spheres (18 nm ± 8 nm, SI 5). The amorphous character is evidenced at reaction times up to 24 s (Fig. 2c) by a broad correlation peak in the 1.5-2 Å^{-1} range assigned to atom-atom correlations, and the absence of Bragg peaks.

During *c.a.* 60 s after mixing, particles remain amorphous while growing: on SAXS patterns (Fig. 2a), the shoulder shifts to lower q values, *i.e.* the particles diameter increases above 100 nm. At larger q values where $I \simeq Bq^{-4}$ (Porod's law), B decreases, evidencing the decrease in the surface-to-volume ratio.[38] After 60 s, Bragg peaks of cerium oxalate appear, and the correlation band at $q_{\text{amorph}} = 1.5$ to 2 Å^{-1} decreases ($I(t) - I(t = 250\,\text{ms}) < 0$ on Fig. 2c), evidencing the consumption of amorphous particles as crystals are formed. The crystallization reaction therefore propagates up to the final crystal size, larger than both the SAXS and WAXS instrumental resolutions, with no evidence of aggregation of transient nanometer-scaled crystals, nor confinement of the reaction by the amorphous nanoparticles as recently observed in oxide nanoparticles.[7,39]

At higher concentrations ([Ce] = 25 mmol L^{-1}), cryoTEM evidences liquid droplets with sizes of several hundreds of nanometers 5 s after mixing (Fig. 1e-g, SI 2.2, tomography Movie SM2.avi). EELS confirms the droplets are rich in cerium and oxygen (Fig. 1h and SI 3.2).

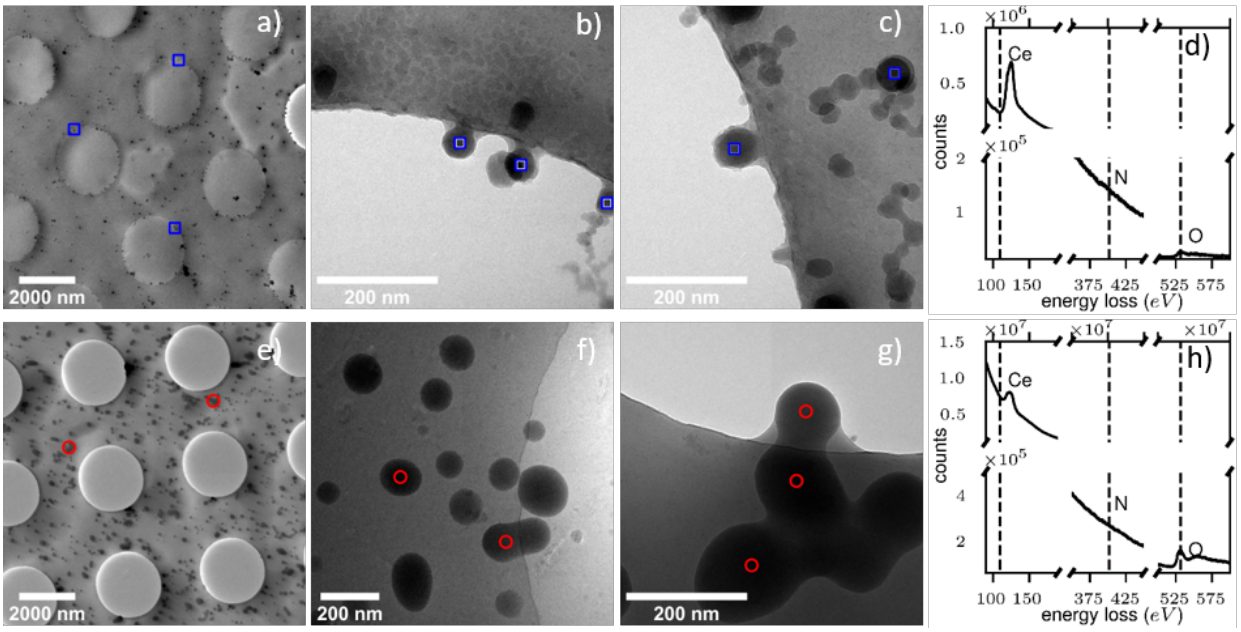

Figure 1: Cryo-TEM images and Electron Energy Loss Spectra of the reacting mixture of cerium nitrate and oxalic acid a-d) [Ce]=1 mmol L^{-1} ($S = 1.4 \times 10^5$, see Methods) 5 s after mixing, e-h) [Ce]=25 mmol L^{-1} ($S = 3.7 \times 10^7$) 5 s after mixing. Only nanometer-scaled particles with rough edges are observed at lower concentrations (□), while particles with non-circular shapes assigned to liquid droplets are predominantly observed at larger concentrations (○).

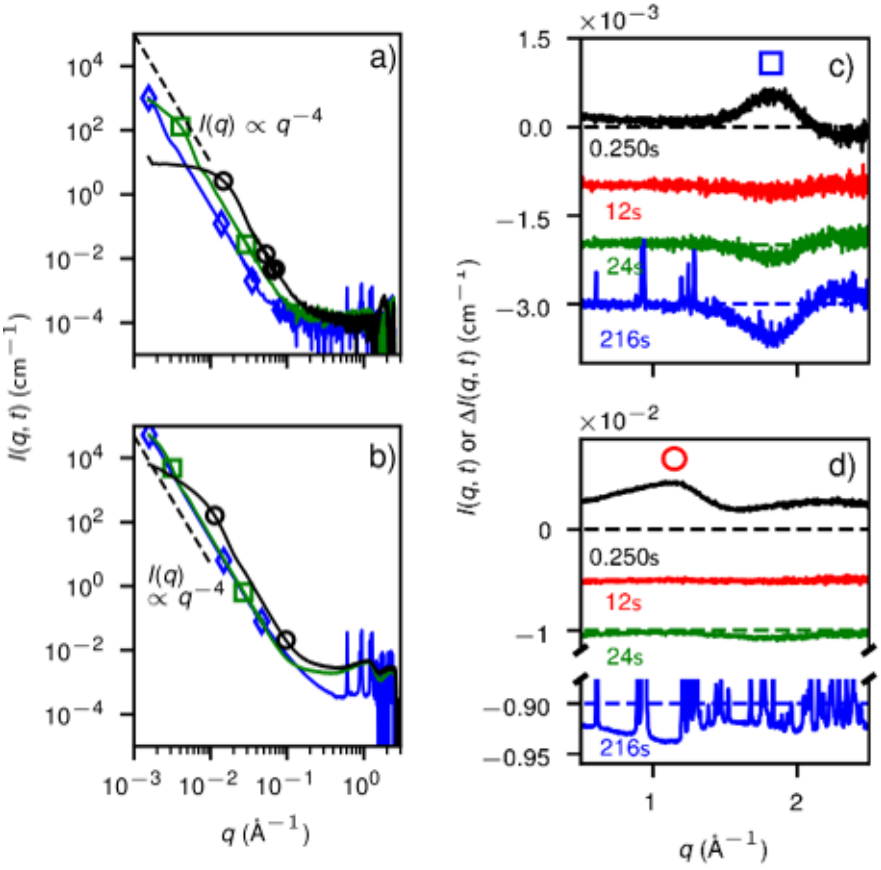

Figure 2: X-ray scattering patterns taken in the 250 ms-216 s range after mixing. Scattered intensity $I(q)$ in the SAXS range with a) [Ce]=1 mmol L^{-1} ($S = 1.4 \times 10^5$) and b) [Ce]=25 mmol L^{-1} ($S = 3.7 \times 10^7$). (-o-): 250 ms. (-□-): 24 s. (-◇-): 216 s. The dashed line indicates a $I \propto q^{-4}$ Porod's law characteristic of smooth, bulk particles. Scattered intensity in the WAXS range, $I(q)$ at 250 ms, and differential intensity $I(t) - I(250\,\text{ms})$, for c) [Ce]=1 mmol L^{-1}, d) [Ce]=25 mmol L^{-1}. (□): signal assigned to the amorphous phase. (○): signal assigned to the reactant-rich liquid phase. WAXS data has been shifted vertically for clarity by an offset value indicated by the dashed lines.

Their liquid state is inferred from their morphology (compare Fig. 1b-c and f-g, SI 2.1and SI 2.2). First, a large fraction of the objects deviates from a spherical shape, while most objects observed at lower cerium concentrations (assigned to amorphous solid particles) are spherical. Among the deformed objects, a significant fraction present non-circular shapes, characteristic of coalescing droplets: most pairs of particles with distances lower that the sum of the radii present a curved shape attributed to a liquid meniscus. The objects at high cerium concentrations are therefore assigned to deformed liquid droplets with lower viscosity and / or lower interfacial tension, while the objects at lower cerium concentrations are assigned to solid amorphous particles, less prone to deformation. These qualitative observations are supported by a statistical analysis (SI 4): at high concentrations ($25\,\mathrm{mmol\,L^{-1}}$), 54% of the objects have a roundness ($4A/\pi L^2$ with A the area and L the major axis) between 0.4 and 0.8, *i.e.* deviate significantly from spherical shapes, as observed qualitatively. Conversely, at low concentrations ($1\,\mathrm{mmol\,L^{-1}}$), 66% of the objects have a roundness in the 0.8 to 1 range, *i.e.* closer to spherical shapes. Second, the shape analysis is supported by an inspection of the interfaces at higher magnifications: the droplets present smooth interfaces, whereas the amorphous particles present significant roughness with characteristic size in the nanometer range.

However, assigning a liquid state from cryoTEM morphology, although common practice for mineral liquid-liquid phase separation,[18,23,31,40] is indirect and prone to error. Although Liu et al. have recently observed identical structures by in situ liquid-cell TEM, they didn't conclude on the liquid nature of the high-concentration structures.[36] Here, we further evidence that two X-ray scattering signatures discriminate reactant-rich liquid droplets from amorphous particles, showing they are two distinct phases, and that the reactant-rich liquid droplets become predominant when the concentration of cerium exceeds 2.5 to $10\,\mathrm{mmol\,L^{-1}}$. First, amorphous particles and liquid droplets have well-defined and different atom-scale structures: up to cerium concentration of $2.5\,\mathrm{mmol\,L^{-1}}$, amorphous particles present a single characteristic WAXS correlation signal ($1.5\,\mathrm{\AA^{-1}} \leq q_{\mathrm{am}} \leq 2\,\mathrm{\AA^{-1}}$, Fig. 2c and SI 6). At cerium

concentrations above $10\,\mathrm{mmol\,L^{-1}}$, droplets present an additional prominent WAXS signal ($0.5\,\mathrm{Å}^{-1} \leq q_{\mathrm{liq}} \leq 1.5\,\mathrm{Å}^{-1}$, Fig. 2d and SI 6) The positions of both WAXS correlation bands are independent of composition (SI 6) and reaction time (Fig. 2c-d), which demonstrates the amorphous and liquid structures are structurally and chemically well-defined and distinct. Although deeper analysis is needed to retrieve the exact atom-atom pair distribution functions,[41,42] it suggests that distances between the stronger X-ray scatterers (presumably cerium atoms) are shorter in the amorphous particles (larger-q correlation peaks) than in the reactant-rich liquid droplets. At longer reaction times, we observe that both the amorphous and liquid phases are converted into cerium oxalate crystals ($I(t) - I(t = 250\,\mathrm{ms}) < 0$ on Fig. 2d).

Second, analysis of the X-ray scattering efficiency per cerium atom (Σ, Fig. 3) further supports that amorphous and liquid structures are distinct thermodynamic phases, and identifies the concentration where the reactant-rich liquid phase becomes predominant. The total scattered intensity ("scattering invariant") normalized by the concentration of cerium is

$$\Sigma = \frac{1}{2\pi^2[\mathrm{Ce}]} \int_0^{+\infty} I(q) q^2 dq \simeq \xi_{\mathrm{am}} v_{\mathrm{am}} \Delta\rho_{\mathrm{am}}^2 + \xi_{\mathrm{liq}} v_{\mathrm{liq}} \Delta\rho_{\mathrm{liq}}^2 \,, \tag{1}$$

where $\xi_{\{\mathrm{am,liq}\}}$ are the molar fractions of cerium in amorphous and liquid structures, $v_{\{\mathrm{am,liq}\}}$ the volumes per cerium atom and $\Delta\rho_{\{\mathrm{am,liq}\}} = \rho_{\{\mathrm{am,liq}\}} - \rho_{\mathrm{H_2O}}$ the differences of scattering length densities of either phase with that of water. Cerium atomsdissolved in water (fraction $\xi_{\mathrm{sol}} = 1 - (\xi_{\mathrm{am}} + \xi_{\mathrm{liq}})$) have no scattering contribution ($\Delta\rho_S = 0$), as we analyze $I(q)$ after subtracting the signal of pure water.

By comparison with WAXS signals, that indicated an onset of liquid formation at cerium concentrations in the 2.5 to $10\,\mathrm{mmol\,L^{-1}}$ range, we conclude that scattering efficiency vary with concentration because the volume fractions of amorphous and liquid phases vary. First, in the 1-10 $\mathrm{mmol\,L^{-1}}$ range, Σ increases (Fig. 3a) while no reactant-rich droplet is observed ($\xi_{\mathrm{liq}} = 0$), evidencing that both the amount of cerium in amorphous particles ($[\mathrm{Ce}]_{\mathrm{am}} = \xi_{\mathrm{am}}[\mathrm{Ce}]$) and the yield of formation of amorphous particles ($\xi_{\mathrm{am}} = [\mathrm{Ce}]_{\mathrm{am}}/[\mathrm{Ce}]$) in-

crease. From the onset of Σ at low concentrations, we estimate the solubility of amorphous particles to be $[\mathrm{Ce}]_{\mathrm{sol}} = 1 \times 10^{-8}$ to $1 \times 10^{-4}\,\mathrm{mol\,L^{-1}}$. Then, at $[\mathrm{Ce}] \simeq 10\,\mathrm{mmol\,L^{-1}}$, the scattering efficiency reaches a maximum $\Sigma^{\max} = \xi_{\mathrm{am}}^{\max} v_{\mathrm{am}} \Delta\rho_{\mathrm{am}}^2$, reflecting the maximal yield of production of amorphous particles. Finally, above $10\,\mathrm{mmol\,L^{-1}}$, Σ decreases, evidencing liquid droplets with lower scattering efficiency are produced at the expense of amorphous particles (ξ_{liq} increases, ξ_{am} decreases, with $v_{\mathrm{liq}}\Delta\rho_{\mathrm{liq}}^2 < v_{\mathrm{am}}\Delta\rho_{\mathrm{am}}^2$). The scattering efficiency reaches a plateau at concentrations above $125\,\mathrm{mmol\,L^{-1}}$, where a pure liquid is expected.

We therefore demonstrate that the amorphous and the liquid phases have well-defined thermodynamic parameters: in addition to the WAXS structure factors, the two characteristic values $v_{\mathrm{liq}}\Delta\rho_{\mathrm{liq}}^2$ and $v_{\mathrm{am}}\Delta\rho_{\mathrm{am}}^2$ are distinct. As they combine molar volume and chemical composition, *via* electron density, we can conclude the amorphous and liquid states are true thermodynamic phases. In particular, the amorphous particles are not in a glass state, *i.e.* can not be considered as solid with a short-range structure identical to that of the liquid.[43] Instead, amorphous particles are presumably denser and less hydrated than liquid droplets, as shown by shorter cerium-cerium distances from the WAXS analysis, and $v_i\Delta\rho_i^2$ values higher for the amorphous particles than for the liquid droplets.

We further clarify the time evolution of the phases: analysis of scattering patterns evidences there is no conversion of reactant-rich droplets into amorphous particles, in contrast to usually reported in other systems.[15,18,23,26,29–31] Here, amorphous particles form at lower reagent concentrations than liquid droplets, which is compatible with the solution being supersaturated first with respect to the lower-solubility amorphous phase, then to the larger-solubility liquid phase. Therefore, one would indeed expect the liquid phase, less stable, to convert with time into the amorphous phase. However, we prove there is no such evolution: the signal assigned to the liquid droplets does not evolve prior up to 12 s (zero WAXS signal in the $0.5\,\mathrm{\AA^{-1}} \leq q_{\mathrm{liq}} \leq 1.5\,\mathrm{\AA^{-1}}$ region, Fig. 2c and d), and the only transformation detected prior to crystallization is a partial dissolution of the amorphous phase after 12 s (negative incremental WAXS signal in the $1.5\,\mathrm{\AA^{-1}} \leq q_{\mathrm{am}} \leq 2\,\mathrm{\AA^{-1}}$ region). The emergence of the liquid

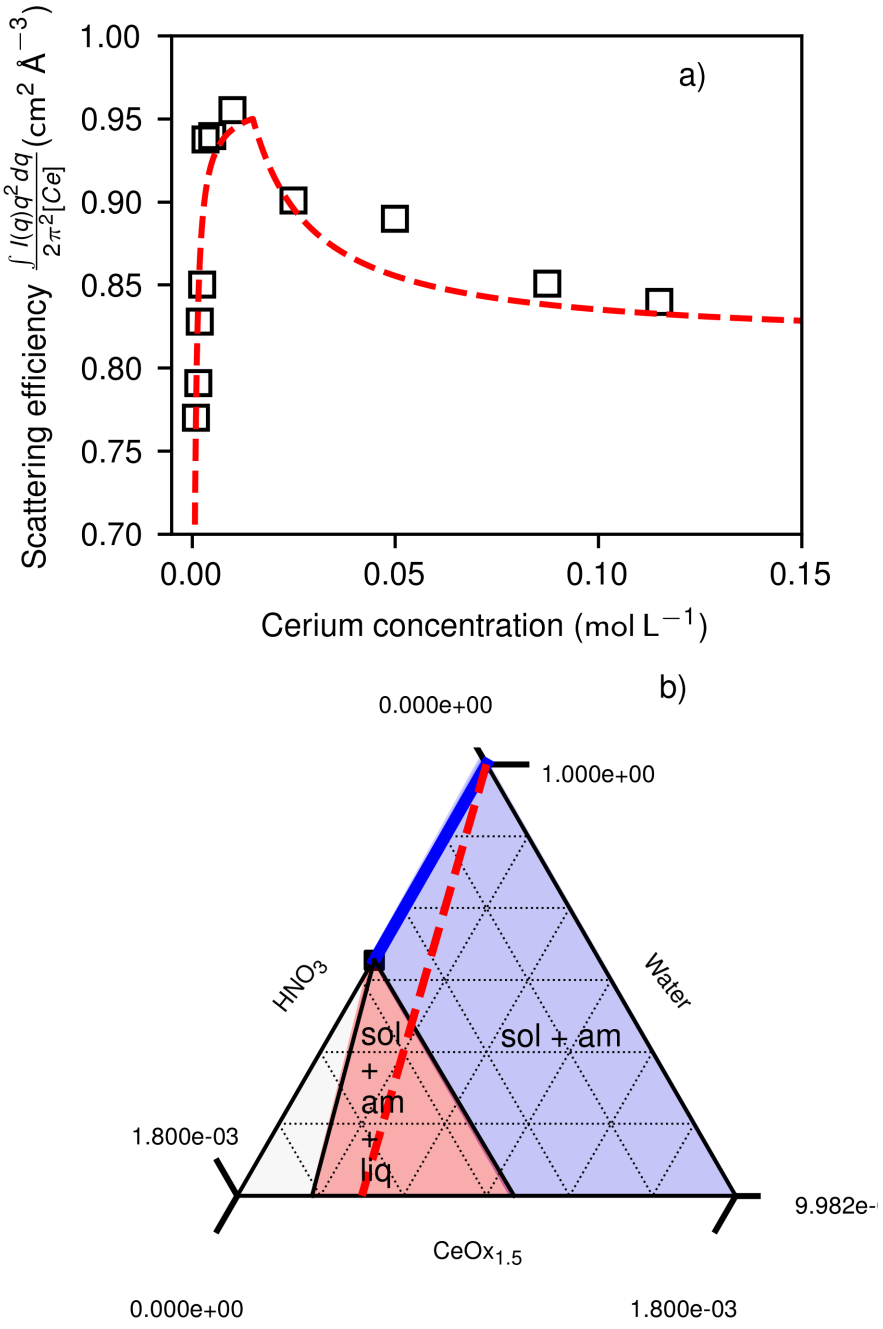

Figure 3: a) scattering efficiency at 250 ms reaction time, from equation 1. (- - - - -) calculated from the phase diagram b) example of a phase diagram compatible with the experimental scattering efficiency.

droplets and their ripening by aggregation is expected to influence the crystallization mechanism. In particular, we show that LLPS favors crystallization by aggregation: Liu *et al.*[36] have indeed reported recently that cerium oxalate forms by classical monomer-by-monomer crystallization at lower concentrations, where we observe formation of amorphous particles followed by dissolution. At larger concentrations, they observe crystallization by aggregation, in the concentration regime where we report LLPS at short reaction times. Such aggregation process is expected for structure that separate from water, and drives crystallization per attachment.

More generally, the lack of conversion from liquid to amorphous structures challenges the usual picture where the liquid forms, then amorphous particles nucleation from the liquid. On the contrary, it suggests that a process faster than 250 ms determines the volume fractions of liquid droplets and amorphous particles. In order to get insight on how volume fractions of each phase $\xi_{\{\mathrm{am,liq}\}}$ are determined, we test their consistency with the lever rule in a multicomponent (more than three) phase diagram. We calculated $\xi_{\{\mathrm{am,liq}\}}$ in ternary phase diagrams where compositions are represented by molar fractions of water, cerium oxalate anhydrate, and nitric acid, and derived the scattering efficiency per Ce atom along a dilution line at constant Ce/oxalic acid = 2/3 ratio (Fig. 3a and b, red lines, SI 7). In particular, taking an amorphous phase (am) of composition $(CeOx_{1.5})(H_2O)_{18.1}$ and molar volume $v_{\mathrm{am}} = 590\,\text{Å}^3$, a reactant-rich liquid (liq) of composition $(CeOx_{1.5})(H_2O)_{23.9}(HNO_3)_{2.9}$ and molar volume $v_{\mathrm{liq}} = 970\,\text{Å}^3$, and a water-rich solution (sol) with $[\mathrm{Ce}] \simeq 2 \times 10^{-4}\,\mathrm{mol\,L^{-1}}$, the phase diagram is consistent with the experimental scattering efficiency: first, the fraction of amorphous phase ξ_{am} increases linearly along the dilution line (dotted line on Fig. 3b) while staying in the binary (sol+am) domain. Then, at $[\mathrm{Ce}] = 10\,\mathrm{mmol\,L^{-1}}$, the system enters the triphasic (sol+am+liq) domain, where the scattering efficiency decreases until the dilution line crosses the (sol+liq) boundary ("pure" liquid phase).

The agreement between experimental and calculated scattering efficiencies supports that the initial volume fraction of each phase is consistent with an underlying phase diagram.

However, the exact compositions and molar volumes of the phases remain unknown: the values given above are one of the many solutions that make experimental and calculated scattering efficiency consistent. Among all possible values, we have selected above molar volumes that are qualitatively consistent with chemical compositions; that is, the molar volume of amorphous and liquid phases are close to those expected from the molar volume of cerium oxalate v_{CeOx}, increased by the volume occupied by the additional water molecules $v_{\mathrm{H_2O}}$ and nitric acid $v_{\mathrm{HNHO_3}}$, *i.e.*

$$v_{(\mathrm{CeOx_{1.5}})(\mathrm{H_2O})_x(\mathrm{HNO_3})_y} = v_{\mathrm{CeOx}} + x v_{\mathrm{H_2O}} + y v_{\mathrm{HNHO_3}} \,. \tag{2}$$

Even with this constraint, multiple solutions are admissible depending on the hypothesis on the solubility of the amorphous phase (SI 7), not to mention that the hypothesis of water and nitric acid incompressibility leading to Eq. 2 could be relaxed.

From the theoretical point of view, the (sol+liq) binodal line is expected in multivalent salts: Monte-Carlo simulations have shown that mixtures of $+z/-z$ ions with size σ in a dielectric continuum ϵ ("restricted primitive model") present a liquid-liquid phase separation with an upper critical temperature $T^* = \frac{4\pi\epsilon\epsilon_0\sigma kT}{(ze)^2} \leq 0.05$ in water.[44] According to this model, for $z \geq 3.7$ an ion-rich liquid should separate at lower temperatures and higher concentrations, *i.e.* at valencies significantly exceeding experimental observations. Still, more complete models that account explicitly for solvent predict phase separations for electrolytes of lower charge, like NaCl and $CaCO_3$.[17,18] Although an exact, quantitative description is reached only when all solvent interactions are taken into account, electrostatic forces combined to the finite size of ions essentially capture liquid-liquid phase separation in the metastable mixture of ionic solutions.

However, a theoretical description is still lacking for the formation of amorphous phases *vs* reactant-rich liquid phases in electrolytes. Nevertheless, amorphous particles are usually considered as a well-defined thermodynamic phase, more stable than the reactant-rich liquid

phase.[15,18,23,26,29–31] Such well-separated thermodynamic parameters motivate the use of the multi-step nucleation theory to describe consecutive nucleation of the amorphous, then the crystal phases, each driven by the chemical potential gradients $\Delta\mu = kT \ln S$ between the respective parent and new phases.[19,45] Here, we demonstrate that the reactant-rich liquid droplets and amorphous particles are indeed well-distinct phases. To account for their co-existence at reaction times of 250 ms, one can first suggest that the two phases nucleate sequentially. However, it would then remain difficult to explain why after the two consecutive separations, the volume fractions of each phase remain constant from 250 ms to c.a. 12 s instead of approaching zero for the first nucleation phase (respectively, unity for the second phase). The situation is clearer after observing that the system is best described by at least three independent chemical species. In this case, at least three phases (the two aggregated phases + dilute solution) may coexist at thermodynamic equilibrium. In the (sol + am + liq) miscibility gap (Fig. 3b), all phases may separate by nucleation and / or spinodal decomposition, following concepts developed for multi-component systems.[46,47] This approach suitably describes why volume fractions remain constant while the system is coarsening, and accounts properly for the variance of the system. Similarly, using a simple binary phase diagram, it is difficult to explain how the most stable phase will dissolve first (the amorphous phase, of lower solubility i.e. higher supersaturation), instead of the least stable phase (the liquid phase, of higher solubility i.e. lower supersaturation), see the vanishing WAXS signals on Fig. 2. However, in a phase diagram with three or more components, as phases start forming the composition of the ion-poor phase (sol) may evolve. A larger number of degrees of freedom allows more complex trajectories in the phase diagram, and qualitatively explains how the more stable phase starts dissolving first. Rationalizing phase transformations based on multivariate phase diagrams is relevant not only for our fundamental understanding of non classical crystallization, but also for practical applications: indeed, we have shown that the concentration threshold before LLPS occurs in cerium oxalate is moderate ([Ce] $\simeq$ 2.5 to 10 mmol L^{-1}), it is prone to be exceeded in laboratory and industrial syntheses where

process intensification is aimed, *e.g.* synthesis of rare earth-based materials, and emerging rare earth recycling processes.[32]

Acknowledgement

We thank Jéril Dégrouard and Amélie Leforestier (Laboratoire de Physique des Solides, Orsay) for their guidance and the access to their cryoTEM to collect preliminary data. The Multimodal Imaging Center of Institut Curie is acknowledged for providing access to cryo-EM facility in Orsay. We acknowledge SOLEIL for provision of synchrotron radiation facilities and we thank Dr Thomas Bizien for assistance in using beamline SWING (proposal 20181790). We acknowledge the financial support of the Energy Division of CEA, the French Alternative Energies and Atomic Energy Commission. We thank Sébastien Teychené, Isaac Rodriguez-Ruiz, Thomas Philippe and Mark Levenstein for stimulating discussions.

Supporting Information Available

The following files are available free of charge.

- `220525-DC-SI_non_classical_nucleation_oxalate.pdf`: Materials and Methods, Supplementary cryo-TEM images, Supplementary EELS spectra and area selections, Statistical analysis of the curvature of the particles, SAXS model fitting and Comparison of the reduced invariant to a ternary phase diagram

- `SM1.avi`: Tomography from cryo-TEM images of a synthesis quenched 5 s after mixing, [Ce] = 1 mmol L^{-1}. The box sizes are 1 µm x 1 µm x 0.15 µm (X, Y, Z).

- `SM2.avi`: Tomography from cryo-TEM images of a synthesis quenched 5 s after mixing, [Ce] = 25 mmol L^{-1}. The box sizes are 1 µm x 1 µm x 0.40 µm (X, Y, Z).

References

(1) Becker, R.; Döring, W. Kinetische Behandlung der Keimbildung in übersättigten Dämpfen. *Annalen der Physik* **1935**, *416*, 719–752.

(2) Kashchiev, D. *Nucleation: Basic Theory With Applications*; Butterworth-Heinemann Ltd: Oxford ; Boston, 2000.

(3) Kelton, K.; Greer, A. L. *Nucleation in condensed matter: applications in materials and biology*; Elsevier: Amsterdam, 2010.

(4) Mullin, J. W. *Crystallization, 4th Edition*; Butterworth-Heinemann: Oxford ; Boston, 2001.

(5) Yoreo, J. J. D.; Gilbert, P. U. P. A.; Sommerdijk, N. A. J. M.; Penn, R. L.; Whitelam, S.; Joester, D.; Zhang, H.; Rimer, J. D.; Navrotsky, A.; Banfield, J. F. et al. Crystallization by particle attachment in synthetic, biogenic, and geologic environments. *Science* **2015**, *349*, aaa6760.

(6) Fleury, B.; Neouze, M.-A.; Guigner, J.-M.; Menguy, N.; Spalla, O.; Gacoin, T.; Carriere, D. Amorphous to Crystal Conversion as a Mechanism Governing the Structure of Luminescent YVO_4:Eu Nanoparticles. *ACS Nano* **2014**, *8*, 2602–2608.

(7) Baumgartner, J.; Ramamoorthy, R. K.; Freitas, A. P.; Neouze, M.-A.; Bennet, M.; Faivre, D.; Carriere, D. Self-Confined Nucleation of Iron Oxide Nanoparticles in a Nanostructured Amorphous Precursor. *Nano Lett.* **2020**,

(8) Rodríguez-Ruiz, I.; Charton, S.; Radajewski, D.; Bizien, T.; Teychené, S. Ultra-fast precipitation of transient amorphous cerium oxalate in concentrated nitric acid media. *CrystEngComm* **2018**, *20*, 3302–3307.

(9) Muschol, M.; Rosenberger, F. Liquid–liquid phase separation in supersaturated

lysozyme solutions and associated precipitate formation/crystallization. *J. Chem. Phys.* **1997**, *107*, 1953–1962.

(10) Berland, C. R.; Thurston, G. M.; Kondo, M.; Broide, M. L.; Pande, J.; Ogun, O.; Benedek, G. B. Solid-liquid phase boundaries of lens protein solutions. *PNAS* **1992**, *89*, 1214–1218.

(11) Galkin, O.; Vekilov, P. G. Control of protein crystal nucleation around the metastable liquid–liquid phase boundary. *PNAS* **2000**, *97*, 6277–6281.

(12) Vivarès, D.; Bonneté, F. Liquid-Liquid Phase Separations in Urate Oxidase/PEG Mixtures: Characterization and Implications for Protein Crystallization. *J. Phys. Chem. B* **2004**, *108*, 6498–6507.

(13) Vivares, D.; Kaler, E. W.; Lenhoff, A. M. Quantitative imaging by confocal scanning fluorescence microscopy of protein crystallization via liquid–liquid phase separation. *Acta Cryst D* **2005**, *61*, 819–825.

(14) Gower, L. B.; Odom, D. J. Deposition of calcium carbonate films by a polymer-induced liquid-precursor (PILP) process. *Journal of Crystal Growth* **2000**, *210*, 719–734.

(15) Sebastiani, F.; Wolf, S. L. P.; Born, B.; Luong, T. Q.; Cölfen, H.; Gebauer, D.; Havenith, M. Water Dynamics from THz Spectroscopy Reveal the Locus of a Liquid–Liquid Binodal Limit in Aqueous $CaCO_3$ Solutions. *Angewandte Chemie International Edition* **2017**, *56*, 490–495.

(16) Smeets, P. J. M.; Finney, A. R.; Habraken, W. J. E. M.; Nudelman, F.; Friedrich, H.; Laven, J.; Yoreo, J. J. D.; Rodger, P. M.; Sommerdijk, N. A. J. M. A classical view on nonclassical nucleation. *PNAS* **2017**, 201700342.

(17) Wallace, A. F.; Hedges, L. O.; Fernandez-Martinez, A.; Raiteri, P.; Gale, J. D.; Waychunas, G. A.; Whitelam, S.; Banfield, J. F.; De Yoreo, J. J. Microscopic Evidence

for Liquid-Liquid Separation in Supersaturated $CaCO_3$ Solutions. *Science* **2013**, *341*, 885–889.

(18) Xu, Y.; Tijssen, K. C. H.; Bomans, P. H. H.; Akiva, A.; Friedrich, H.; Kentgens, A. P. M.; Sommerdijk, N. A. J. M. Microscopic structure of the polymer-induced liquid precursor for calcium carbonate. *Nature Communications* **2018**, *9*, 2582.

(19) G. Vekilov, P. The two-step mechanism of nucleation of crystals in solution. *Nanoscale* **2010**, *2*, 2346–2357.

(20) Kashchiev, D. Classical nucleation theory approach to two-step nucleation of crystals. *Journal of Crystal Growth* **2020**, *530*, 125300.

(21) Haberkorn, H.; Franke, D.; Frechen, T.; Goesele, W.; Rieger, J. Early stages of particle formation in precipitation reactions—quinacridone and boehmite as generic examples. *Journal of Colloid and Interface Science* **2003**, *259*, 112–126.

(22) Rieger, J.; Frechen, T.; Cox, G.; Heckmann, W.; Schmidt, C.; Thieme, J. Precursor structures in the crystallization/precipitation processes of $CaCO_3$ and control of particle formation by polyelectrolytes. *Faraday Discuss.* **2007**, *136*, 265–277.

(23) Faatz, M.; Gröhn, F.; Wegner, G. Amorphous Calcium Carbonate: Synthesis and Potential Intermediate in Biomineralization. *Advanced Materials* **2004**, *16*, 996–1000.

(24) Wolf, S. E.; Leiterer, J.; Kappl, M.; Emmerling, F.; Tremel, W. Early Homogenous Amorphous Precursor Stages of Calcium Carbonate and Subsequent Crystal Growth in Levitated Droplets. *J. Am. Chem. Soc.* **2008**, *130*, 12342–12347.

(25) Wolf, S. E.; Müller, L.; Barrea, R.; Kampf, C. J.; Leiterer, J.; Panne, U.; Hoffmann, T.; Emmerling, F.; Tremel, W. Carbonate-coordinated metal complexes precede the formation of liquid amorphous mineral emulsions of divalent metal carbonates. *Nanoscale* **2011**, *3*, 1158–1165.

(26) Bewernitz, M. A.; Gebauer, D.; Long, J.; Cölfen, H.; Gower, L. B. A metastable liquid precursor phase of calcium carbonate and its interactions with polyaspartate. *Faraday Discuss.* **2013**, *159*, 291–312.

(27) Rodriguez-Navarro, C.; Kudłacz, K.; Cizer, O.; Ruiz-Agudo, E. Formation of amorphous calcium carbonate and its transformation into mesostructured calcite. *CrystEngComm* **2014**, *17*, 58–72.

(28) Zou, Z.; Habraken, W. J. E. M.; Bertinetti, L.; Politi, Y.; Gal, A.; Weiner, S.; Addadi, L.; Fratzl, P. On the Phase Diagram of Calcium Carbonate Solutions. *Advanced Materials Interfaces* **2017**, *4*, 1600076.

(29) Avaro, J. T.; Wolf, S. L. P.; Hauser, K.; Gebauer, D. Stable Prenucleation Calcium Carbonate Clusters Define Liquid–Liquid Phase Separation. *Angewandte Chemie International Edition* **2020**, *59*, 6155–6159.

(30) Gebauer, D.; Kellermeier, M.; Gale, J. D.; Bergström, L.; Cölfen, H. Pre-Nucleation Clusters as Solute Precursors in Crystallisation. *Chem. Soc. Rev.* **2014**, *43*, 2348–2371.

(31) Loh, N. D.; Sen, S.; Bosman, M.; Tan, S. F.; Zhong, J.; Nijhuis, C. A.; Král, P.; Matsudaira, P.; Mirsaidov, U. Multistep Nucleation of Nanocrystals in Aqueous Solution. *Nat Chem* **2017**, *9*, 77–82.

(32) Binnemans, K.; Jones, P. T.; Blanpain, B.; Van Gerven, T.; Yang, Y.; Walton, A.; Buchert, M. Recycling of rare earths: a critical review. *Journal of Cleaner Production* **2013**, *51*, 1–22.

(33) Charton, S.; Kacem, A.; Amokrane, A.; Borda, G.; Puel, F.; Klein, J.-P. Actinides Oxalate Precipitation in Emulsion Modeling: From the Drop Scale to the Industrial Process. *Chemical Engineering Research and Design* **2013**, *91*, 660–669.

(34) Pang, H.; Chen, C. Facile Synthesis of Cerium Oxide Nanostructures for Rechargeable Lithium Battery Electrode Materials. *RSC Adv.* **2014**, *4*, 14872–14878.

(35) Tyrpekl, V.; Markova, P.; Dopita, M.; Brázda, P.; Vacca, M. A. Cerium Oxalate Morphotypes: Synthesis and Conversion into Nanocrystalline Oxide. *Inorg. Chem.* **2019**, *58*, 10111–10118.

(36) Liu, L.; Kruska, K.; Hall, G. B.; Clark, R. A.; Meier, D. E.; Buck, E. C. Formation and growth of cerium (III) oxalate nanocrystals by liquid-cell transmission electron microscopy. *Scripta Materialia* **2022**, *219*, 114856.

(37) Han, J.; Testard, F.; Malloggi, F.; Coulon, P.-E.; Menguy, N.; Spalla, O. Understanding of the Size Control of Biocompatible Gold Nanoparticles in Millifluidic Channels. *Langmuir* **2012**, *28*, 15966–15974.

(38) Lindner, P., Zemb, T., Eds. *Neutrons, X-rays and light: scattering methods applied to soft condensed matter*, 1st ed.; North-Holland delta series; Norh-Holland, Elsevier: Amsterdam, 2002.

(39) Freitas, A. P.; Ramamoorthy, R. K.; Durelle, M.; Larquet, E.; Maurin, I.; Testard, F.; Chevallard, C.; Gacoin, T.; Carriere, D. Crystallization within Intermediate Amorphous Phases Determines the Polycrystallinity of Nanoparticles from Coprecipitation. *Nano Lett.* **2022**, *22*, 29–35.

(40) Gindele, M. B.; Steingrube, L. V.; Gebauer, D. Generality of liquid precursor phases in gas diffusion-based calcium carbonate synthesis. *CrystEngComm* **2021**, *23*, 7938–7943.

(41) Ramamoorthy, R. K.; Levesque, M.; Belloni, L.; Carriere, D. Structure Factor of EuCl3 Aqueous Solutions via Coupled Molecular Dynamics Simulations and Integral Equations. *J. Phys. Chem. B* **2020**, *124*, 1787–1793.

(42) Fetisov, E. O.; Mundy, C. J.; Schenter, G. K.; Benmore, C. J.; Fulton, J. L.; Kathmann, S. M. Nanometer-Scale Correlations in Aqueous Salt Solutions. *J. Phys. Chem. Lett.* **2020**, 2598–2604.

(43) Debenedetti, P. G. *Metastable Liquids – Concepts and Principles*; Princeton University Press: Princeton, N.J, 1997.

(44) Orkoulas, G.; Panagiotopoulos, A. Z. Free energy and phase equilibria for the restricted primitive model of ionic fluids from Monte Carlo simulations. *J. Chem. Phys.* **1994**, *101*, 1452–1459.

(45) Kashchiev, D.; Vekilov, P. G.; Kolomeisky, A. B. Kinetics of Two-Step Nucleation of Crystals. *J. Chem. Phys.* **2005**, *122*, 244706.

(46) Petrishcheva, E.; Abart, R. Exsolution by spinodal decomposition in multicomponent mineral solutions. *Acta Materialia* **2012**, *60*, 5481–5493.

(47) Gutzow, I. S.; Schmelzer, J. W. *The Vitreous State*; Springer Berlin Heidelberg: Berlin, Heidelberg, 2013.